



## TECHNICAL REPORTS: DATA

10.1002/2014EA000061

### Key Points:

- Ion temperatures are calculated from TWINS energetic neutral atom data
- Maps of ion temperatures during geomagnetic storms are available on CDAWeb

### Correspondence to:

A. M. Keesee,  
amy.keese@mail.wvu.edu

### Citation:

Keesee A. M., and Scime E. E. (2015)  
Database of ion temperature maps  
during geomagnetic storms, *Earth  
and Space Science*, 2, 39–46,  
doi:10.1002/2014EA000061.

Received 2 DEC 2014

Accepted 27 JAN 2015

Accepted article online 3 FEB 2015

Published online 25 FEB 2015

This is an open access article under the terms of the Creative Commons Attribution-NonCommercial-NoDerivs License, which permits use and distribution in any medium, provided the original work is properly cited, the use is non-commercial and no modifications or adaptations are made.

## Database of ion temperature maps during geomagnetic storms

Amy M. Keesee<sup>1</sup> and Earl E. Scime<sup>1</sup>

<sup>1</sup>Department of Physics and Astronomy, West Virginia University, Morgantown, West Virginia, USA

**Abstract** Ion temperatures as a function of the  $x$  and  $y$  axes in the geocentric solar magnetospheric (GSM) coordinate system and time are available for 76 geomagnetic storms that occurred during the period July 2008 to December 2013 on CDAWeb. The method for mapping energetic neutral atom data from the Two Wide-angle Imaging Spectrometers (TWINS) mission to the GSM equatorial plane and subsequent ion temperature calculation are described here. The ion temperatures are a measure of the average thermal energy of the bulk ion population in the 1–40 keV energy range. These temperatures are useful for studies of ion dynamics, for placing in situ measurements in a global context, and for establishing boundary conditions for models of the inner magnetosphere and the plasma sheet.

### 1. Introduction

Ion temperature measurements help us to understand the dynamics of ions in the magnetosphere and the underlying physical processes that control the observed ion heating and dynamics. For example, observations of a dawn-dusk asymmetry in the plasma sheet ion temperatures [e.g., *Eastman et al.*, 1985; *Wang et al.*, 2012] led to an understanding of how ions move in the near-Earth tail under the influence of the energy-dependent curvature-gradient drift [*Spence and Kivelson*, 1993]. In other studies, ion temperatures were found to increase during geomagnetic storms [*Baumjohann et al.*, 1989] and substorms [*Baumjohann et al.*, 1991], demonstrating that processes such as adiabatic heating and magnetic reconnection occur during these active periods. The ion temperature, along with ion density, is a key parameter needed to establish accurate boundary conditions for inner magnetospheric modeling of ion populations. Thus, the ability to measure ion temperatures with spatial and temporal resolution is important to improving our understanding of magnetospheric dynamics. Calculation of ion temperatures from energetic neutral atom (ENA) data provides such measurements over the inner magnetosphere and plasma sheet with a time resolution approaching a few minutes.

The Two Wide-angle Imaging Neutral-atom Spectrometers (TWINS) mission [*McComas et al.*, 2009] is a NASA Explorer Mission of Opportunity in which identical instruments have been placed on two satellites in Molniya orbits with apogees of  $\sim 7.2 R_E$  and  $63.4^\circ$  inclinations. The satellites complete two orbits per day with alternating apogees, enabling near-continuous observational coverage. The satellites are three-axis stabilized with the instruments mounted on an approximately nadir pointing surface. Each instrument includes an energetic neutral atom imager on a scanning platform, a Lyman  $\alpha$  monitor, and environmental sensors that detect the local charged particle environment. The ENA imager is based on the Medium Energy Neutral Atom (MENA) instrument [*Pollock et al.*, 2000] developed for the Imager for Magnetopause-to-Aurora Global Experiment (IMAGE) mission [*Burch*, 2000]. The TWINS ENA imager includes two time-of-flight (TOF) resolving sensor heads that are offset by  $\pm 15^\circ$  to provide a one-dimensional view of  $\sim 140^\circ$ . The second spatial dimension is obtained by a rotating actuator to yield a full image in 60 s. The ENA imager observes 1–100 keV ENAs with  $\sim 4^\circ \times 4^\circ$  angular and  $\sim 1$  min time resolution. Data are available from June 2008 through the present time.

The remote ion temperature calculation technique was originally established using data from MENA [*Scime et al.*, 2002]. Ion temperatures were calculated for each pixel in the instrument coordinates, known as the “skymap” view. Ion temperatures derived from these line-of-sight ENA measurements were shown to be in excellent agreement with in situ ion temperatures measured by the Magnetospheric Plasma Analyzer (MPA) instruments on geosynchronous satellites flown by Los Alamos National Laboratory (LANL); when those satellites were in the path of the ENA line of sight. *Scime et al.* [2002] observed a consistent dawn-dusk asymmetry in ion temperatures, with cooler temperatures near dawn, during several storm periods.

Orbital motion and precession make it difficult to compare data from different times or consider long-time averages. Thus, *Zaniewski et al.* [2006] developed a method of mapping the ENA flux along the instrument line of sight (LOS) to the equatorial plane in geocentric solar magnetospheric (GSM) coordinates. Using a superposed epoch analysis, they demonstrated that ions are injected on the nightside, near midnight, but that the hottest ions are located near noon during the main phase of storms.

*Keesee et al.* [2008] calculated the ion temperatures as a function of distance from Earth and of time during the evolution of a geomagnetic storm. They observed periodic heating that coincided with the occurrence of a series of periodic substorms. They also found that ENA-derived ion temperatures matched those calculated with a model based on solar wind velocity during certain intervals of the storm but found much higher ion temperatures during other intervals, specifically those with the substorms. Thus, solar wind-based models, which are often used to establish boundary conditions for inner magnetospheric models, will miss important ion heating events.

These techniques have been further developed and applied to data from the Two Wide-angle Neutral atom Spectrometers (TWINS) mission. A calculation of average ion temperatures for quiet conditions over a period of 2 months demonstrated the dawn-dusk asymmetry in the magnetotail predicted by the *Spence and Kivelson* [1993] model describing the effect of the energy-dependent curvature-gradient drift [*Keesee et al.*, 2011]. A study using TWINS-derived ion temperatures during a high-speed stream-driven storm included observations of storm time ion heating, convection of hot ions into the inner magnetosphere, and a region of hot ions near midnight in the magnetotail that could be associated with bursty bulk flows [*Keesee et al.*, 2012]. Superposed epoch analysis of storm time ion temperatures calculated from TWINS data showed that ion temperatures increase during the main phase of intense coronal mass ejection-driven storms, while for high-speed stream-driven storms ion temperatures increase during the recovery phase and such storms tend to have higher dayside than nightside temperatures on average [*Keesee et al.*, 2014a]. Regions of ion energization have been observed using this technique during the extreme substorm that has been associated with the loss of the Galaxy-15 spacecraft. Some observed regions were consistent with the narrow extent of localized flow channels, while others were patchy and more consistent with a current-disruption substorm model [*Keesee et al.*, 2014b].

The TWINS ion temperatures have been used to establish boundary conditions for inner magnetospheric models. *Elfritz et al.* [2014] conducted comparative simulations of the Comprehensive Ring Current Model (CRCM) between ion temperature boundary conditions established from TWINS data and from the *Tsyganenko and Mukai* [2003] model. They demonstrated that the ion temperature and the convection strength play a dual role in determining the dynamics of the inner magnetosphere. TWINS ion temperatures are also being used for boundary conditions in the Rice Convection Model-Equilibrium (RCM-E) [*Keesee et al.*, 2014b].

In this paper we describe the method used for calculating ion temperatures throughout the duration of 76 geomagnetic storms during the period June 2008 to December 2013 and the details of the data that are available on CDAWeb (<http://cdaweb.gsfc.nasa.gov/>).

## 2. Data Selection and Analysis

Geomagnetic storms are identified by the minimum value of the disturbance storm time (*Dst*) index having a magnitude greater than 40 nT using the Kyoto site. During the period under consideration, 79 storms have been identified. Three storms were discarded due to lack of TWINS data or issues with orbital and attitude data. The remaining 76 storms have been analyzed from 12 h prior to *Dst* minimum to 24 h following *Dst* minimum. Table 1 gives details of the storms. Some data are available for dates not listed in Table 1 due to events that were analyzed but later had their minimum *Dst* revised with magnitude lower than 40 nT. The ENA data are divided into 20 sweep (~25 min) averages. ENA data are sorted into actuation angle, polar angle, and TOF bins using a detailed model of the instrument response. Under the assumption that all ENAs are hydrogen, TOF bins are converted to energy bins with  $\Delta E/E = 1$  (e.g., a bin with central energy of 12 keV includes energies from 6 keV to 18 keV). Statistics-based spatial smoothing and background subtraction algorithms are applied to the data [see *McComas et al.*, 2011, Appendix]. Nineteen energy bins with central energies ranging from 2 to 60 keV are calculated, while the 13 lowest energy bins, with central energies from 2 to 32 keV, are used for the ion temperature calculation to avoid uncertainties introduced by using higher energy bins that have flux levels close to the noise floor.

**Table 1.** List of Storms Identified With Minimum *Dst* Having a Magnitude of at Least 40 nT<sup>a</sup>

Date	Minimum <i>Dst</i> (nT)	Time of Minimum <i>Dst</i> (UT) <sup>b</sup>	Storm Driver
15-Jun-2008	-41	5:00	HSS
4-Sep-2008	-51	4:00	HSS
11-Oct-2008	-54	11:00	HSS
4-Feb-2009 <sup>c</sup>	-42	18:00	CME
22-Jul-2009	-83	6:00	HSS
23-Oct-2009	-47	2:00	CME
15-Feb-2010	-58	22:00	CME
6-Apr-2010	-81	14:00	CME
12-Apr-2010	-51	1:00	CME
2-May-2010	-66	17:00	HSS
29-May-2010	-85	13:00	CME
4-Jun-2010	-47	1:00	HSS
4-Aug-2010	-67	4:00	CME
11-Oct-2010	-80	18:00	CME
28-Dec-2010	-50	16:00	CME
4-Feb-2011	-59	21:00	CME + HSS
1-Mar-2011	-81	14:00	HSS
11-Mar-2011	-83	5:00	CME + HSS
6-Apr-2011	-65	18:00	CME + HSS
12-Apr-2011	-51	9:00	HSS
28-May-2011	-91	11:00	CME + HSS
1-Jul-2011	-44	7:00	HSS
5-Jul-2011	-50	0:00	nighttime substorm
6-Aug-2011	-107	3:00	CME + HSS
9-Sep-2011	-70	15:00	CME + HSS
17-Sep-2011	-70	15:00	CME
26-Sep-2011	-101	23:00	CME
25-Oct-2011	-132	1:00	CME
1-Nov-2011	-72	15:00	transient
30-Nov-2011	-44	18:00	SSBC, sus. SWBz
23-Jan-2012	-69	5:00	CME
25-Jan-2012	-73	10:00	CME
15-Feb-2012	-58	16:00	CME
19-Feb-2012	-54	4:00	HSS
27-Feb-2012	-48	19:00	CME
7-Mar-2012	-74	9:00	CME
9-Mar-2012	-131	8:00	CME w/sus. SWBz
12-Mar-2012	-50	16:00	CME
15-Mar-2012	-74	20:00	CME
28-Mar-2012	-55	4:00	HSS w/sus. SWBz
5-Apr-2012	-54	7:00	sus. SWBz
13-Apr-2012	-49	4:00	HSS
24-Apr-2012 <sup>c</sup>	-102	4:00	CME
9-May-2012	-41	9:00	HSS
23-May-2012	-47	4:00	HSS
12-Jun-2012	-51	1:00	sus. SWBz
17-Jun-2012	-71	13:00	CME
9-Jul-2012	-68	12:00	CME
15-Jul-2012	-127	18:00	CME
3-Sep-2012	-74	10:00	CME
1-Oct-2012	-119	4:00	CME
9-Oct-2012 <sup>c</sup>	-105	8:00	CME
13-Oct-2012	-87	7:00	HSS
1-Nov-2012	-62	20:00	CME
14-Nov-2012	-108	7:00	CME + HSS
17-Jan-2013	-53	22:00	CME
26-Jan-2013	-51	22:00	HSS
1-Mar-2013	-55	10:00	HSS
17-Mar-2013	-132	20:00	CME
29-Mar-2013	-60	16:00	HSS
24-Apr-2013	-49	18:00	HSS

**Table 1.** (continued)

Date	Minimum <i>Dst</i> (nT)	Time of Minimum <i>Dst</i> (UT) <sup>b</sup>	Storm Driver
1-May-2013	-67	18:00	HSS
18-May-2013	-57	4:00	CME
25-May-2013	-55	6:00	CME + HSS
1-Jun-2013	-119	8:00	CME + HSS
7-Jun-2013	-73	5:00	HSS
29-Jun-2013	-98	6:00	HSS + transient
6-Jul-2013	-79	18:00	CME
10-Jul-2013	-47	21:00	CME
14-Jul-2013	-72	22:00	sus. SWBz
27-Aug-2013	-54	21:00	SSBC
2-Oct-2013	-67	7:00	CME
9-Oct-2013	-65	1:00	CME
15-Oct-2013	-45	3:00	HSS
30-Oct-2013	-52	23:00	CME
7-Nov-2013	-54	12:00	HSS + SSBC
9-Nov-2013	-81	8:00	HSS
11-Nov-2013	-70	7:00	HSS
8-Dec-2013	-66	8:00	HSS

<sup>a</sup>CME = coronal mass ejection. HSS = high speed stream, SSBC = solar sector boundary crossing, sus. SWBz = sustained southward interplanetary magnetic field Bz.

<sup>b</sup>Note that the Kyoto *Dst* times are indicated from 1–24 h UT, but we have converted these to a 0:00–23:00 UT scale.

<sup>c</sup>Events for which the TWINS flux or orbital and attitude data had issues.

### 3. Mapping to GSM Equatorial Plane

The orbital motion of the spacecraft yields a constantly changing field of view (FOV) that makes it difficult to compare data from different times or consider long-time averages. To create a consistent viewing orientation, ENA flux data are projected along the instrument line of sight (LOS) to a grid of  $0.5 \times 0.5 R_E$  bins in the equatorial plane of the geocentric solar magnetospheric (GSM) coordinate system that extends  $-60 R_E < x < 20 R_E$  and  $-40 R_E < y < 40 R_E$ . Any ENA flux that is projected to bins that fall outside a modeled magnetosphere boundary [Shue *et al.*, 1997] is ignored. Specifically, the LOS is calculated for each of the four corners of a given pixel. The locations of the intersections of the four LOSs with the GSM equatorial plane define a two-dimensional FOV in the plane. If the FOV falls within a single bin, then all ENA flux from that pixel is assigned to that bin. For pixels with FOVs that overlap multiple bins, the fraction of FOV area that overlaps a given bin is calculated and that fraction of ENA flux from that pixel is assigned to the bin. For

example, if a quarter of a pixel's FOV overlaps a spatial bin, then a quarter of that pixel's ENA flux is assigned to that bin. The remaining ENA flux is divided among the remaining bins that are overlapped by the FOV in a similar manner. A counting array is used to track each time a bin is populated with ENA flux from a pixel, and the total ENA flux in a given bin is divided by the number of times that bin has been populated to yield an average ENA flux. A sample counting array is shown in Figure 1.

Based on instrument geometry, the size of the FOV overlapping with the equatorial plane increases with distance from the Earth. Thus, pixels near the Earth tend to be populated with ENA flux from multiple instrument pixels

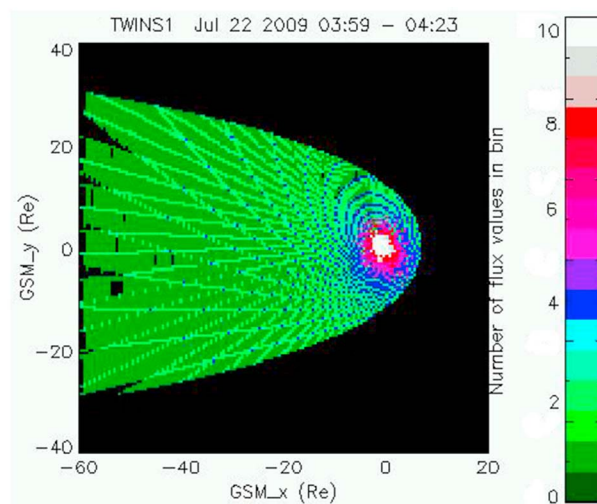


**Figure 1.** Counting array of the number of times that each bin has been populated by projected ENA flux from an instrument pixel.

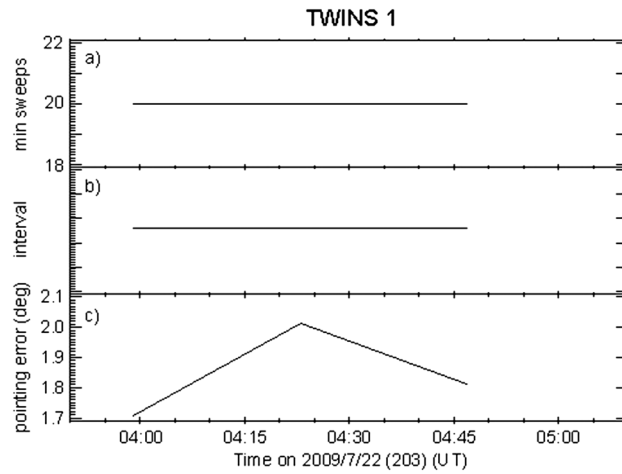


**Figure 2.** Line plots of (a) minimum number of sweeps in a data interval, (b) time coverage of available data (y axis value is arbitrary), and (c) uncertainty in the angle that gives the direction in which the TWINS instrument is pointing for 3:50–5:10 UT on 22 July 2009.

while the FOV of one instrument pixel overlaps multiple bins further from the Earth. This can be seen in Figure 1 where bins that are far from the Earth are populated by ENA flux from one instrument pixel, except in the bins where the LOSs from the corners of four instrument pixels intersect. In contrast, the number of times the bins near the Earth are populated is beyond the scale of the color bar.

ENA studies that focus on ion populations of the inner magnetosphere typically use a magnetic field model to determine the source location of the measured ENA flux. These techniques include deconvolution [Perez et al., 2012], forward modeling [Brandt et al., 2001], and a LOS mapping technique [Roelof, 1997]. In the latter technique,

the point of closest approach of the LOS to the Earth is mapped to the equator along a modeled magnetic field line, assuming that the point of closest approach will have the highest geocoronal density, thus yielding the highest ENA flux. However, most of our studies have focused on plasma sheet populations, which are also appropriate for inner magnetosphere boundary conditions. For LOSs that intersect the equatorial plane in the plasma sheet from satellite locations on the dayside, a magnetic field model would map the point of closest approach much further downtail where the ion density is much lower, yielding much lower ENA flux. If instead, the point of intersection of the LOS with the equatorial plane is mapped back to the Earth along a modeled magnetic field line, then that magnetic field line would intersect the LOS at a point close to the point of closest approach. Thus, the geocoronal density would only be slightly less, yielding nearly the same ENA emission. Therefore, the technique described here which is independent of a magnetic field model yields a good approximation of the source location of the flux that dominates the ENA measurement.

#### 4. Ion Temperature Calculation

ENAs are created when an energetic ion and a cold neutral atom undergo a charge exchange collision. During such a collision, the path deflection and energy loss are minimal such that the ENA retains many properties of the parent ion. The measured ENA intensity,  $j_{ENA}$  (with units of  $(\text{cm}^2 \text{sr s eV})^{-1}$ ), is a convolution of the ion distribution function,  $j_{ion}$ , and the energy-dependent charge exchange cross section given by

$$j_{ENA}(E, \vec{u}) = \sigma_{cx}(E) \int_0^{\vec{R}} \left( n_n(\vec{r}(s)) j_{ion}(\vec{r}(s), E, \vec{u}) \exp\left(-\int_0^{\vec{r}(s)} \alpha(s') ds'\right) \right) ds. \quad (1)$$

The integral is performed along the LOS from the location of ENA emission,  $\vec{r}$ , to the location of the satellite,  $\vec{R}$ , with  $\vec{r}(s) = \vec{r} + \vec{u} s$  and  $\vec{u}$  is a unit vector along the LOS;  $\sigma_{cx}$  is the energy-dependent charge exchange cross section [Freeman and Jones, 1974]; and  $n_n$  is the neutral density. The integral over  $\alpha(s')$  accounts for attenuation of ENAs due to additional collisions or ionization of the ENA, which is approximately zero where such collisions are minimal. For measurements from within  $5^\circ$  of the limb of the Earth this approximation is not valid, so they are removed from the images.

If the parent ion distribution is a Maxwellian, then the high-energy portion of the spectrum (energies greater than the ion temperature) is dominated by emission from the hottest region along the LOS [Hutchinson, 1987].

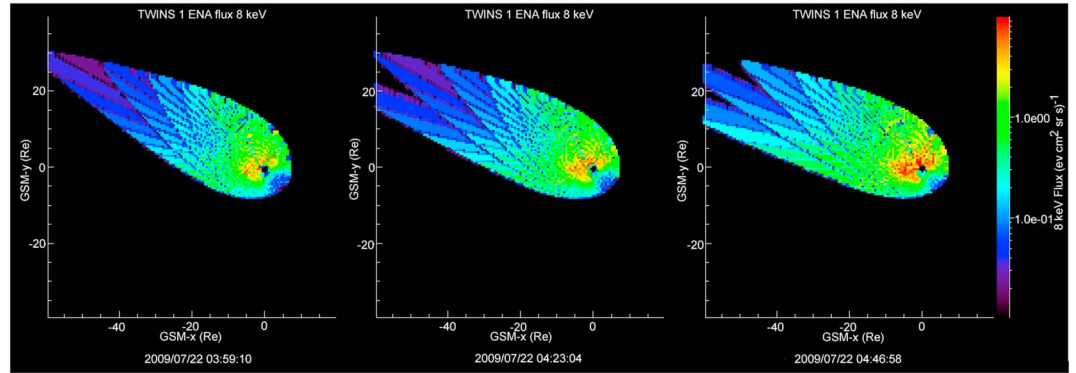


**Figure 3.** ENA flux at 8 keV projected to the GSM equatorial plane (Sun is to the right) for three consecutive intervals during 3:50–5:10 UT on 22 July 2009.

We approximate the integral by the value of the integrand at the hottest location,  $s^*$ , multiplied by a characteristic length along  $s$ ,  $\zeta$  [Scime and Hokin, 1992], to obtain

$$j_{ENA} \approx \sigma_{cx}(E)\zeta n_n(s^*) j_{ion}(s^*, E). \tag{2}$$

By projecting along the LOS to the equatorial plane, we are assuming that the hottest region lies in the equatorial plane, a valid assumption for plasma sheet populations in the near-Earth magnetotail [Hughes, 1995]. Plugging in a Maxwellian distribution yields

$$\frac{j_{ENA}}{\sigma_{cx}(E)E} \approx \frac{\zeta n_n(s^*) n_i(s^*)}{\sqrt{2m_i} (\pi T_i(s^*))^{3/2}} \exp\left(\frac{-E}{T_i(s^*)}\right). \tag{3}$$

For each spatial bin in the GSM equatorial plane grid, the average ENA flux obtained from the LOS projection is divided by the charge exchange cross section multiplied by the energy. This energy spectrum is fit to equation (3) to obtain an ion temperature value for that spatial bin. For bins that do not yield a fit, the temperature is set to zero. This process yields an ion temperature map that is a function of  $x$  and  $y$  in GSM coordinates, and a map is generated for each time step during the storms.

### 5. Database Details and Example Plots

To access the data on CDAWeb, select TWINS from the list of sources. On the Data Selector page, select TWINS1\_TISTORM\_IMAGER and TWINS2\_TISTORM\_IMAGER. TWINS1 and TWINS2 indicate each of the TWINS satellites. Each of the available Variable Parameters listed on the Data Explorer page are described below,

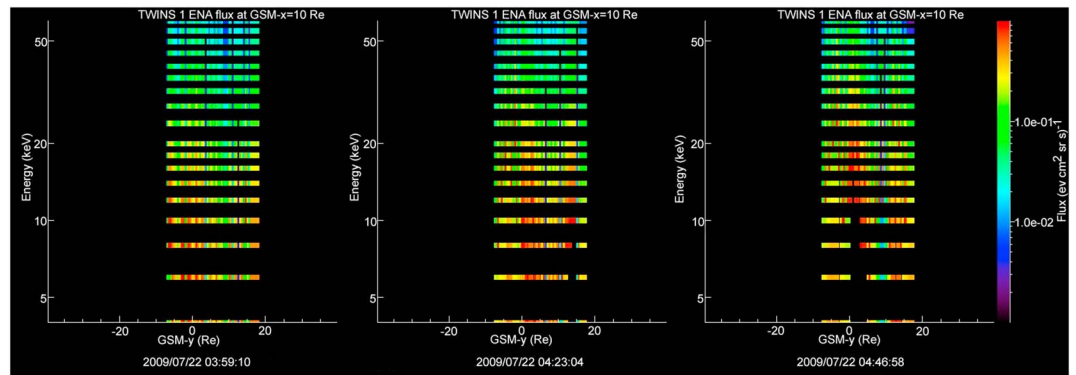


**Figure 4.** Spectrogram plots of projected ENA flux versus energy (along the vertical axis ranging from 2 to 60 keV) and GSM  $y$  axis (along the horizontal axis ranging from  $-40$  to  $40 R_E$ ) for a cut at  $x = 10 R_E$  for three consecutive intervals during 3:50–5:10 UT on 22 July 2009.

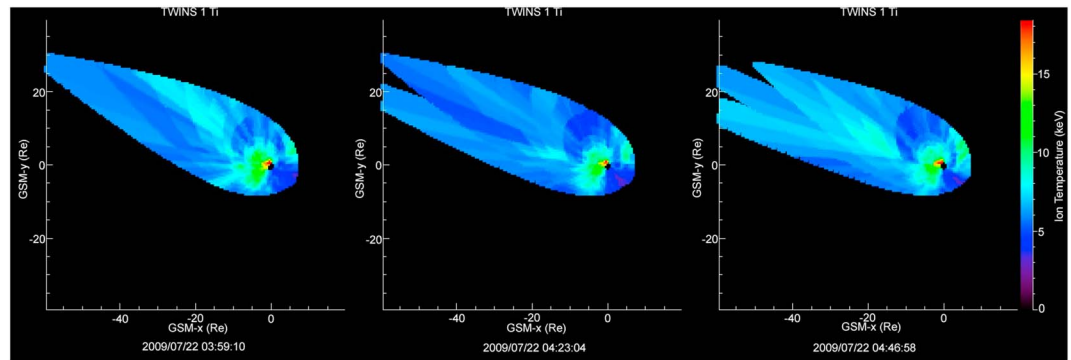


**Figure 5.** Plots of calculated ion temperature in the GSM equatorial plane for three consecutive intervals during 3:50–5:10 UT on 22 July 2009.

in order of appearance on the site. Example plots from CDAWeb cover 3:50–5:10 UT on 2009 July 22, which was included in the analysis of this event described in Keesee *et al.* [2012].

The number of TWINS sweeps used—minimum/maximum will always be 20 for both values in this data set. This indicates that every interval includes an average of 20 actuator sweeps. These values are displayed as a line plot, as shown in Figure 2a.

Plots of the average ENA flux images projected to the GSM  $xy$  plane are available for seven central energies of 2, 8, 14, 20, 24, 32, and 45 keV. Example plots of ENA flux at 8 keV for three consecutive intervals are shown in Figure 3. Spectrograms of ENA flux versus energy and one spatial dimension are available along the GSM  $y$  axis for GSM  $x$  axis values of 10 and 20  $R_E$  and along the GSM  $x$  axis for GSM  $y$  axis values of  $-5$  and  $5 R_E$ . Examples for a cut at  $x = 10 R_E$  are shown in Figure 4. Movies of the projected ENA flux images and spectrograms are also available.

The ion temperature images calculated from the projected ENA fluxes, as described in section 4 for each time interval, along with movies of these images as a function of time, are available. Examples of ion temperature images are shown in Figure 5. The time interval used for the ion temperature calculation gives a line plot showing the time coverage of the available data, as shown in Figure 2b. The regular  $\sim 4.5$  h intervals between data are times when the instrument is turned off while the satellite moves through perigee. At these times, coverage is generally provided by the other instrument. The uncertainty in the angle that gives the direction in which the TWINS instrument is pointing is also given in a line plot, as shown in Figure 2c. When this angle is greater than the  $4^\circ$  spatial resolution used, it will introduce additional uncertainty in the projected location.

## 6. Conclusions

We have analyzed TWINS ENA data to calculate ion temperatures during the evolution of 76 geomagnetic storms during the June 2008 to December 2013 period. We have described the method of analysis and the details of what data are available. The ion temperatures are available to the public at CDAWeb (<http://cdaweb.gsfc.nasa.gov/>). We hope that the community will find these ion temperatures useful for studies of ion dynamics during geomagnetic storms, to place in situ measurements in a global context, and as boundary conditions for inner magnetospheric modeling.

## References

- Baumjohann, W., G. Paschmann, and C. Cattell (1989), Average plasma properties in the central plasma sheet, *J. Geophys. Res.*, *94*, 6597–6606, doi:10.1029/JA094iA06p06597.
- Baumjohann, W., G. Paschmann, T. Nagai, and H. Luhr (1991), Superposed epoch analysis of the substorm plasma sheet, *J. Geophys. Res.*, *96*, 605–608.
- Brandt, P., S. Barabash, E. C. Roelof, and C. Chase (2001), Energetic neutral atom imaging at low altitudes from the Swedish microsatellite Astrid: Extraction of the equatorial ion distribution, *J. Geophys. Res.*, *106*, 25,731–25,744, doi:10.1029/2000JA900023.
- Burch, J. L. (2000), Image mission overview, *Space Sci. Rev.*, *91*, 1–14.
- Eastman, T. E., L. A. Frank, and C. Y. Huang (1985), The boundary layers as the primary transport regions of the Earth's magnetotail, *J. Geophys. Res.*, *90*, 9541–9560, doi:10.1029/JA090iA10p09541.

### Acknowledgments

This work was carried out as a part of the TWINS NASA Explorer mission, supported under subcontract 799104L to the Southwest Research Institute, NASA EPSCoR grant NNX10AN08A, and NSF grant AGS-1113478. We would like to thank Dieter Bilitza and Bob McGuire for assistance with transferring the data to CDAWeb and the TWINS Science Team for helpful discussions regarding TWINS data analysis. TWINS data are available at <http://twins.swri.edu/> and the ion temperatures discussed are available at <http://cdaweb.gsfc.nasa.gov/>. IDL scripts used to analyze the data can be obtained by contacting A.M. Keesee at [amy.keesee@mail.wvu.edu](mailto:amy.keesee@mail.wvu.edu).

- Elfritz, J., A. Keesee, N. Buzulukova, M.-C. Fok, and E. E. Scime (2014), First results using TWINS-derived ion temperature boundary conditions in CRISM, *J. Geophys. Res. Space Physics*, *119*, 3345–3361, doi:10.1002/2013JA019555.
- Freeman, R. L., and E. M. Jones, (1974), Atomic collision processes in plasma physics experiments, CLM-R 137, 1, Culham Lab., Culham, U. K.
- Hughes, W. J. (1995), The magnetopause, magnetotail, and magnetic reconnection, in *Introduction to Space Physics*, edited by M. G. Kivelson, and C. T. Russell, pp. 227–287, Cambridge Univ. Press, New York.
- Hutchinson, I. H. (1987), *Principles of Plasma Diagnostics*, Cambridge Univ. Press, Cambridge, U. K.
- Keesee, A. M., E. Scime, and M. B. Moldwin (2008), Remote measurements of ion temperatures in the terrestrial magnetotail, *J. Geophys. Res.*, *113*, A00A03, doi:10.1029/2008JA013130.
- Keesee, A. M., N. Buzulukova, J. Goldstein, D. J. McComas, E. E. Scime, H. Spence, M. C. Fok, and K. Tallaksen (2011), Remote observations of ion temperatures in the quiet time magnetosphere, *Geophys. Res. Lett.*, *38*, L03104, doi:10.1029/2010GL045987.
- Keesee, A. M., J. G. Elfritz, D. J. McComas, and E. E. Scime (2012), Inner magnetosphere convection and magnetotail structure of hot ions imaged by ENA during a HSS-driven storm, *J. Geophys. Res.*, *117*, A00L06, doi:10.1029/2011JA017319.
- Keesee, A. M., M. W. Chen, E. E. Scime, and A. T. Y. Lui (2014a), Regions of ion energization observed during the Galaxy-15 substorm with TWINS, *J. Geophys. Res. Space Physics*, *119*, 8274–8287, doi:10.1002/2014JA020466.
- Keesee, A. M., J. G. Elfritz, M.-C. Fok, D. J. McComas, and E. E. Scime (2014b), Superposed epoch analyses of ion temperatures during CME- and CIR/HSS-driven storms, *J. Atmos. Sol. Terr. Phys.*, *115–116*, 67–78, doi:10.1016/j.jastp.2013.08.009.
- McComas, D. J., et al. (2009), The Two Wide-angle Imaging Neutral-atom Spectrometers (TWINS) NASA Mission-of-Opportunity, *Space Sci. Rev.*, *142*(1–4), 157–231, doi:10.1007/s11214-008-9467-4.
- McComas, D. J., et al. (2011), First IBEX observations of the terrestrial plasma sheet and a possible disconnection event, *J. Geophys. Res.*, *116*, A02211, doi:10.1029/2010JA016138.
- Perez, J. D., E. W. Grimes, J. Goldstein, D. J. McComas, P. Valek, and N. Billor (2012), Evolution of CIR storm on 22 July 2009, *J. Geophys. Res.*, *117*, A09221, doi:10.1029/2012JA017572.
- Pollock, C., et al. (2000), Medium Energy Neutral Atom (MENA) imager for the IMAGE mission, *Space Sci. Rev.*, *91*, 113–154.
- Scime, E. E., and S. Hokin (1992), Design and calibration of a fast time resolution charge exchange analyzer, *Rev. Sci. Instrum.*, *63*, 4527.
- Roelof, E. (1997), Energetic neutral atom imaging of magnetospheric ions from high- and low-altitude spacecraft, *Adv. Space Res.*, *20*(3), 341–350, doi:10.1016/S0273-1177(97)00689-3.
- Scime, E. E., A. M. Keesee, J.-M. Jahn, J. L. Kline, C. J. Pollock, and M. Thomsen (2002), Remote ion temperature measurements of Earth's magnetosphere: Medium energy neutral atom (MENA) images, *Geophys. Res. Lett.*, *29*(10), 1438, doi:10.1029/2001GL013994.
- Shue, J.-H., J. K. Chao, H. C. Fu, C. T. Russell, P. Song, K. K. Khurana, and H. J. Singer (1997), A new functional form to study the solar wind control of the magnetopause size and shape, *J. Geophys. Res.*, *102*, 9497–9511, doi:10.1029/97JA00196.
- Spence, H. E., and M. Kivelson (1993), Contributions of the low-latitude boundary layer to the finite width magnetotail convection model, *J. Geophys. Res.*, *98*, 15,487–15,496, doi:10.1029/93JA01531.
- Tsyganenko, N. A., and T. Mukai (2003), Tail plasma sheet models derived from Geotail particle data, *J. Geophys. Res.*, *108*(A3), 1136, doi:10.1029/2002JA009707.
- Wang, C.-P., M. Gkioulidou, L. R. Lyons, and V. Angelopoulos (2012), Spatial distributions of the ion to electron temperature ratio in the magnetosheath and plasma sheet, *J. Geophys. Res.*, *117*, A08215, doi:10.1029/2012JA017658.
- Zaniewski, A. M., X. Sun, A. Gripper, E. E. Scime, J.-M. Jahn, and C. J. Pollock (2006), Evolution of remotely measured inner magnetospheric ion temperatures during a geomagnetic storm, *J. Geophys. Res.*, *111*, A10221, doi:10.1029/2006JA011769.